Global Biogeochemical Cycles

RESEARCH ARTICLE
10.1029/2020GB006538

Key Points:

- Surface waters have a large range in dissolved silicon isotopes covering nutrient-rich coastal upwelling to oligotrophic waters
- Deep water masses with DSi concentrations >100 μmol kg^{-1} show homogenous silicon isotope signatures despite up to 25 μmol kg^{-1} differences in [DSi]
- Hydrothermal fluids have a negligible effect on Si isotope distributions in the deep Pacific

Supporting Information:

- Supporting Information S1

Correspondence to:
P. Grasse and M. A. Brzezinski,
patricia.grasse@idiv.de;
mark.brzezinski@lifesci.uscb.edu

Citation:
Grasse, P., Closset, I., Jones, J. L., Geilert, S., & Brzezinski, M. A. (2020). Controls on dissolved silicon isotopes along the U.S. GEOTRACES Eastern Pacific Zonal Transect (GP16). *Global Biogeochemical Cycles*, *34*, e2020GB006538. https://doi.org/10.1029/2020GB006538

Received 10 JAN 2020
Accepted 3 AUG 2020
Accepted article online 6 AUG 2020

Controls on Dissolved Silicon Isotopes Along the U.S. GEOTRACES Eastern Pacific Zonal Transect (GP16)

P. Grasse[1,2], **I. Closset**[3], **J. L. Jones**[3], **S. Geilert**[2], **and M. A. Brzezinski**[3]

[1]German Centre for integrative Biodiversity Research (iDiv), Leipzig, Germany, [2]GEOMAR, Helmholtz Centre for Ocean Research Kiel, Ocean Circulation and Climate Dynamics, Kiel, Germany, [3]Marine Science Institute and the Department of Ecology, Evolution, and Marine Biology, University of California, Santa Barbara, CA, USA

Abstract The distribution of dissolved silicon isotopes (δ^{30}Si) was examined along the U.S. GEOTRACES East Pacific Zonal Transect (GP16) extending from Peru to Tahiti (10°S and 15°S latitude). Surface waters in the subtropical gyre displayed high δ^{30}Si due to strong utilization of silicic acid (DSi). In contrast, surface waters close to the Peruvian coast where upwelling prevailed were less depleted and only moderately fractionated. δ^{30}Si of water masses along the transect was compared with the results of an Optimum Multiparameter Analysis that quantified the fractional contributions of end-member water masses in each sample. Strong admixture of intermediate waters obscured the expected heavy isotopic signatures of Subantarctic Mode Water and Antarctic Intermediate Water. Isotope values were nearly homogenous below 2,000 m (average: +1.3 ± 0.1‰, 1 s.d.) despite the 25 μmol kg^{-1} range in the DSi content among water masses. This homogeneity confirms prior observations and model results that predict nearly constant δ^{30}Si values of +1.0‰ to +1.2‰ for Pacific deep waters with [DSi] > 100 μmol kg^{-1}. Waters above the East Pacific Rise (EPR) influenced by hydrothermal activity showed a small increase in [DSi] together with dissolved iron, but overall stations close to the EPR were slightly depleted in [DSi] (3 to 6 μmol kg^{-1}) with no significant shift in δ^{30}Si compared to adjacent waters. Hydrothermal [DSi] appears to precipitate within the conduit of the EPR or upon contact with cold seawater resulting in a negligible influence of hydrothermal fluids on δ^{30}Si in deep water.

1. Introduction

Silicic acid, $Si(OH)_4$, hereafter referred to as dissolved silicon (DSi), is one of the major macronutrients in the ocean along with nitrate (NO_3^-) and orthophosphate (PO_4^{3-}). Diatoms, which account for 40% of marine primary productivity, have a strict growth requirement for DSi that they use to build their cell wall (e.g., P. Tréguer et al., 2017; Werner, 1977). Therefore, DSi plays an essential role in oceanic primary productivity and is closely linked to the carbon cycle, especially in coastal upwelling areas, where diatoms dominate the phytoplankton community (e.g., Nelson et al., 1995; P. Tréguer et al., 2017). The isotopic composition of DSi (δ^{30}Si) has proven to be a powerful tool to better understand the role of DSi and diatoms in ocean processes as the δ^{30}Si of seawater carries information about DSi utilization in surface waters, the subsequent dissolution of sinking biogenic silica (hereafter referred to as BSi), as well as water mass mixing (e.g., De La Rocha et al., 1997; Grasse et al., 2013; B. Reynolds et al., 2006).

The U.S. GEOTRACES East Pacific Zonal Transect (EPZT, GP16) that extended from the coast of Peru to Tahiti between 10°S and 15°S latitude afforded the opportunity to examine Si isotope dynamics along a strong gradient in surface productivity and in a region where models predict relatively homogenous δ^{30}Si among deep water masses (de Souza et al., 2014; Gao et al., 2016). The coastal end-member of the EPZT along the Peruvian coast is a major upwelling system with high productivity induced by Ekman suction of nutrient-rich subsurface waters with high PO_4^{3-}, DSi, and total dissolved iron (dFe) concentrations (e.g., Bruland et al., 2005). The export of plankton and its decomposition at depth produces one of the largest subsurface oxygen minimum zones (OMZs) in the global ocean (Karstensen et al., 2008; Pennington et al., 2006). High primary productivity along the coast with chlorophyll concentrations (Chl *a*) of 5–10 mg m^{-3} (Echevin et al., 2008) strongly contrasts with the South Pacific subtropical gyre offshore that are some of the most oligotrophic and "clearest" waters in the world ocean with Chl *a* as low as 0.02 mg m^{-3} (Morel et al., 2010).

Along the EPZT subsurface water masses are a complex mix of waters originating from both the south and the north (Peters, Jenkins, et al., 2018). Antarctic Intermediate Water (AAIW), Circumpolar Deep Water (CDW), and Antarctic Bottom Water (AABW) originate in the Southern Ocean. Relatively high DSi utilization in AAIW formation regions and DSi trapping within CDW and AABW in the Southern Ocean are predicted to partition heavy isotopes of Si to AAIW with the deep water masses retaining light isotopes (de Souza et al., 2014; Gao et al., 2016; Holzer & Brzezinski, 2015). Northern water masses in the upper 1,500 m include Equatorial Subsurface Water (ESSW) and Equatorial Pacific Intermediate Water (EqPIW) with Pacific Deep Water (PDW) found at depth. PDW is marked by having one of the highest DSi concentrations in the global ocean. All deep waters >2,000 m have [DSi] over 120 μmol kg^{-1}. Models predict little variation in $\delta^{30}Si$ when [DSi] exceeds ~100 μmol kg^{-1} (e.g., B. C. Reynolds, 2009; Wischmeyer et al., 2003), leading to the hypothesis of a homogenous deep Si isotope distribution along the EPZT.

The main factor controlling $\delta^{30}Si$ in the euphotic zone is DSi utilization by diatoms, which preferentially incorporate the lighter Si isotopes into their frustules, elevating the $\delta^{30}Si$ of the surrounding seawater (e.g., De La Rocha et al., 1997). Culture studies have shown that the fractionation factor ($^{30}\varepsilon$) between diatoms and seawater is −0.5‰ to −2.1‰ (mean −1.0 ± 0.4‰, 1 s.d.) depending on the diatom species (De La Rocha et al., 1997; J. N. Sutton et al., 2013) and possibly iron limitation (Meyerink et al., 2017). $^{30}\varepsilon$ is independent of temperature (12–22°C; De La Rocha et al., 1997), pCO_2 concentrations (Milligan et al., 2004), and growth rate (Sun et al., 2014). Silica dissolution in the euphotic zone may counter the effect of production. Several studies investigated Si isotope fractionation during dissolution ($^{30}\varepsilon_{Diss}$) of diatom frustules (Demarest et al., 2009; Sun et al., 2014; Wetzel et al., 2014) with $^{30}\varepsilon_{Diss}$ ranging from 0‰ to +0.9‰. Thus, in the euphotic zone, $\delta^{30}Si$ is driven to higher values by silica production and possibly to lower values by silica dissolution. These effects are expected to vary geographically, with higher dissolution to production ratios ($\int$D:P) in oligotrophic regions (~80%) and lower ratios in productive coastal zones, where on average, 15% of the produced silica is dissolved within the euphotic zone (Brzezinski et al., 2003; Nelson et al., 1995; Nelson & Brzezinski, 1997).

Below the euphotic zone, silica production is negligible, but silica dissolution continues resulting in the loss of about half of the BSi that is exported out of the euphotic zone in deep waters (Holzer et al., 2014; P. J. Tréguer & De La Rocha, 2013). The fraction of BSi production that is buried in sediments is thought to be balanced by a combination of riverine input (P. J. Tréguer & De La Rocha, 2013) and benthic fluxes that results from dissolution of BSi and silicate alteration at the sediment-water interface (Ehlert et al., 2012; Grasse et al., 2016) and input from hydrothermal sources with low $\delta^{30}Si$ (~ −0.3‰; De La Rocha et al., 2000). However, the influence of benthic fluxes, including hydrothermal input of Si, on $\delta^{30}Si$ in the deep ocean is not well constrained.

Models have revealed a close coupling between biological fractionation, silica export, and dissolution and the meridional overturning circulation (de Souza et al., 2014; Gao et al., 2016; Holzer & Brzezinski, 2015) and are generally highly successful at reproducing the global observations of $\delta^{30}Si$. The Pacific is the exception. Whereas models predict the deep Pacific to have nearly homogenous $\delta^{30}Si$ across the entire basin (de Souza et al., 2014; Gao et al., 2016; B. C. Reynolds, 2009; Wischmeyer et al., 2003), observations indicate a more complex pattern. A wide range in $\delta^{30}Si$ values have been reported for the deep Pacific Ocean (>2,000 m) ranging from low $\delta^{30}Si$ values (+0.6‰) in the North Pacific (De La Rocha et al., 2000; B. Reynolds et al., 2006) to high $\delta^{30}Si$ values (+1.7‰; mean: +1.5‰; Jones, personal communication, 17.05.2019; Beucher et al., 2008) in the Cascadia Basin, which possibly results from additional sources like the Northeast Pacific DSi Plume (Johnson et al., 2006). The flux of Si required to sustain the plume is large (1.5 Tmol Si yr^{-1}) and equivalent to a third of that supplied to the global ocean by rivers (Johnson et al., 2006). However, inputs, like the Northeast Pacific Si Plume or hydrothermal sources, have not been implemented in marine Si models, so their influence on the $\delta^{30}Si$ in deep waters is uncertain. This is a significant issue as benthic DSi fluxes from the seafloor are estimated to be 10 times higher than the inputs of DSi from rivers (~70 Tmol Si yr^{-1} vs. with ~7 Tmol Si yr^{-1}; P. J. Tréguer & De La Rocha, 2013).

Today, the spatial resolution of $\delta^{30}Si$ data in the Pacific is inadequate to evaluate mechanisms leading to even the first-order distribution of isotopes of Si in the basin. In order to better understand those mechanisms, seawater samples from the international GEOTRACES program along the EPZT (GP16) transect

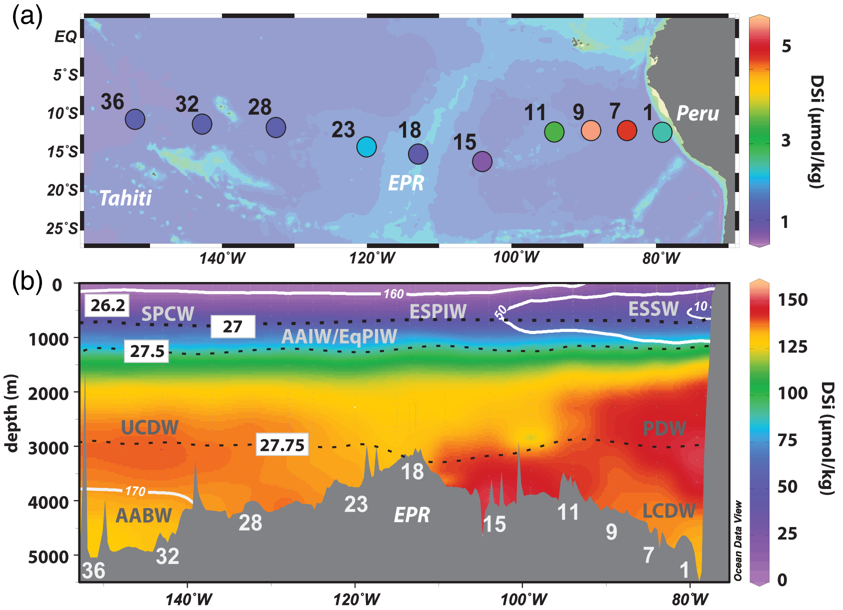

Figure 1. (a) GP16 transect with sampling locations. [DSi] in the surface water is shown in μmol kg^{-1}. (b) [DSi] (in μmol kg^{-1}) along the section and water masses according to Peters, Jenkins, et al. (2018). Surface and subsurface water masses are Eastern South Pacific Intermediate Water (ESPIW), South Pacific Central Water (SPCW), and Equatorial Subsurface Water (ESSW). The main intermediate water masses at approximately 1,000 m depth are Equatorial Pacific Intermediate Water (EqPIW) and Antarctic Intermediate Water (AAIW). Deep water masses are Upper Circumpolar Deep Water (UCDW), Antarctic Bottom Water (AABW), Lower Circumpolar Deep Water (LCDW), and Pacific Deep Water (PDW). Potential density lines (σ_θ; kg m^{-3}) are indicated by dashed black lines and oxygen concentrations (μmol kg^{-1}) with solid white lines. Station numbers as well as the location of the East Pacific Rise (EPR) are shown at the bottom of (b). ODV plots are created using Schlitzer (2018).

from Peru to Tahiti were analyzed. Sampling spanned a large gradient in primary productivity from the upwelling region off Peru to the oligotrophic subtropical gyre near Tahiti reflecting different levels of diatom productivity and silica ∫D:P ratios. The transect also sampled the region's strong OMZ and several intermediate and deep water masses whose isotopic signatures have been predicted from observations and models. Finally, the section offers the ability to evaluate the influence of the hydrothermal plume from the East Pacific Rise (EPR) on the deep δ^{30}Si distribution.

2. Materials and Methods

2.1. Sampling

The U.S. GEOTRACES GP16 transect was conducted on board the *R/V* Thomas G. Thompson from October 2013 until December 2013. The transect extended from Peru to Tahiti (79°W to 152°W) between 10°S and 15°S (Figure 1a). Seawater samples for δ^{30}Si measurements were collected at 10 full stations using the Oceanographic Data Facility's (ODF, Scripps Institution of Oceanography) CTD rosette mounted with Niskin samplers and a Sea-Bird Electronics CTD (SBE9*plus*). Nutrient analyses were performed on a Seal Analytical continuous-flow AutoAnalyzer (AA3) onboard the *R/V* Thompson. Nutrient measurements as well as reference nutrient seawater (RMNS) were performed according to Atlas et al. (1971) and Gordon et al. (1992). For details, see Peters, Jenkins, et al. (2018). Nutrient and hydrographic data are available through the Biological and Chemical Oceanography Data Management Office Website (https://www.bco-dmo.org/project/499723) and from the GEOTRACES Intermediate Data Product (IDP; Schlitzer et al., 2018). Seawater samples for δ^{30}Si measurements were gravity filtered into polypropylene containers through in-line Supor filter capsules (0.8/0.45 μm) attached directly to each Niskin bottle. Sample bottles were capped and stored without preservative in the dark. A detailed description of the physical and biogeochemical environment (nutrients and oxygen concentrations), as well as water mass contributions according to an Optimum Multiparameter Analysis (OMPA), can be found in Peters, Jenkins, et al. (2018).

2.2. Sample Preparation and Si Isotope Measurements

Sample preparation and $\delta^{30}Si$ measurements were conducted in two different laboratories (GEOMAR Helmholtz Centre for Ocean Research Kiel, Germany, and the University of California, Santa Barbara (UCSB), USA). Samples with low [DSi] (<20 μmol kg^{-1}) were measured at GEOMAR and high [DSi] (>20 μmol kg^{-1}) at UCSB due to the higher sample mass requirement for the methods used at UCSB. Intercalibration was accomplished through the analysis of a subset of 25 samples by each laboratory, representing between one and four samples from all stations with DSi concentrations ranging from 5.5 to 107.1 μmol kg^{-1} (supporting information Tables S1 and S2). Additionally, the seawater standards $ALOHA_{300}$ and $ALOHA_{1000}$ as well as solid reference materials (Big Batch [BB] and Diatomite) were monitored at both laboratories during the measurements. For samples that were measured at both laboratories the $\delta^{30}Si$ mean of all single measurements (GEOMAR and UCSB) is given with the corresponding 2 s.d. error (see Table S1). $\delta^{30}Si$ data are available through the Biological and Chemical Oceanography Data Management Office Website (https://www.bco-dmo.org/dataset/728819).

2.2.1. GEOMAR

The pH of samples was raised with NaOH to precipitate $Mg(OH)_2$ to scavenge DSi (MAGIC, B. Reynolds et al., 2006, after Karl & Tien, 1992). The precipitate was isolated by centrifugation, dissolved in HCl, and diluted to a final concentration of ~2 ppm Si. Residual seawater cations were removed by passing each concentrate through AG50W-X8 (200–400 mesh) resin. Samples were analyzed using an Aridus II nebulizer coupled to a Nu Plasma MC-ICP-MS (Nu Instruments™, Wrexham, UK). Each analysis involved 50 to 60 cycles in sample-standard bracketing mode against NBS28. Details of sample preparation are presented in Grasse et al. (2013). Samples were repeated two to four times in different analytical sessions (n = analytical replicate) with a few exceptions that were only measured once (Table S1). Among the samples more than 50% were full replicates that included the MAGIC precipitation step and column chemistry. Sample reproducibility (2 s.d.) was generally between 0.01‰ and 0.26‰, except for one sample with 0.32‰ (2 s.d.). The standards $ALOHA_{1000}$ and $ALOHA_{300}$ resulted in +1.27 ± 0.15‰ (mean ± 2 s.d., $n = 35$) and +1.80 ± 0.22‰ ($n = 10$), respectively, which are in good agreement with values obtained by the GEOTRACES intercalibration study from Grasse et al. (2017; +1.24 ± 0.20‰; +1.68 ± 0.35‰, mean ± 2 s.d.). Solid reference standards (BB and Diatomite) resulted in a mean $\delta^{30}Si$ of −10.56 ± 0.26‰ (2 s.d., $n = 12$) and +1.25 ± 0.14‰ (2 s.d., $n = 9$), which are in very good agreement with consensus values (B. C. Reynolds et al., 2007). For more details including the median for standards, see Table S3.

2.2.2. UCSB

Seawater samples for isotopic analysis were processed following the method described in Brzezinski et al. (2006). The method involved the quantitative precipitation of silicon from seawater as trimethylamine silicomolybdate using a high-purity triethlyamine ammonium molybdate solution (TEA-Moly). The precipitate was isolated by filtration onto a polycarbonate filter and purified by high temperature combustion to produce solid silicon dioxide (SiO_2, De La Rocha et al., 1996). SiO_2 was then converted to Cs_2SiF_6 by dissolution in HF and addition of CsCl. The Cs_2SiF_6 was decomposed with 98% sulfuric acid to generate SiF_4 gas that was cryogenically purified and analyzed in a modified Kiel III inlet system coupled to a gas source MAT252 Isotope Ratio Mass Spectrometer (IRMS). Samples were run against cryogenically purified commercial SiF_4 gas using a sample-standard bracketing approach (20 cycles per analysis). The final $\delta^{30}Si$ sample value was calculated according to Paul et al. (2007) using a multiple-point normalization procedure, that is, based on the linear relationship between the consensus values and measured $\delta^{30}Si$ values of two or more reference standards (in this study NBS28, BB, and Diatomite) to achieve a more constrained calibration of the reference SiF_4 gas. With the multiple-point normalization the value of NBS28 is dictated by the regression line for all standards rather than assumed to be zero as in the single-point normalization. This did not bias the result from the two laboratories as the value for NBS28 from the multiple-point normalization procedure is +0.03 ± 0.19‰ (2 s.d.), which is well within analytical uncertainty (see below).

Measurements were generally repeated two to four times in different analytical sessions (see Table S1). Reproducibility of $\delta^{30}Si$ analyses averages ±0.16‰ (2 s.d.) for samples and ±0.12‰ (2 s.d.) for standards. Accuracy of measurements was checked using intercalibrated seawater standards $ALOHA_{1000}$ ($\delta^{30}Si$ = +1.29 ± 0.22‰; $n = 35$) and $ALOHA_{300}$ (+1.44 ± 0.28‰; $n = 12$) and solid reference standards (BB: −10.50 ± 0.21‰ [$n = 120$] and Diatomite: +1.26 ± 0.20‰ [$n = 25$]). Standard values above are

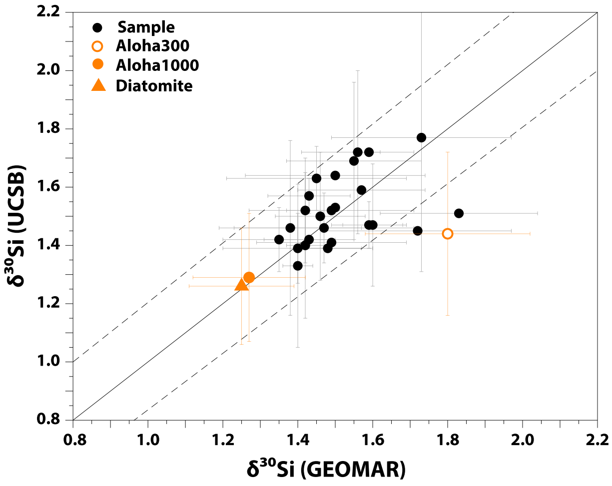

Figure 2. $\delta^{30}Si_{UCSB}$ versus $\delta^{30}Si_{GEOMAR}$ data for samples (black symbols) and standards (orange symbols) including a 1:1 line (solid black line) with a .2‰ error (2 s.d., dashed line) for better comparison of the intercalibrated data. Note that, for clarity, the Big Batch value is not shown but falls on a 1:1 line (see Table S3).

reported as mean values with 2 s.d. The values obtained for all standard and reference materials are in good agreement with the intercalibrated values published by Grasse et al. (2017) and B. C. Reynolds et al. (2007). For more details including the median for standards, see Table S3.

3. Results

3.1. Analytical Calibration Between GEOMAR and UCSB

The comparison between samples ($n = 25$) and standard measurements from both laboratories shows that, despite the use of different sample processing methods (MAGIC vs. TEA-Moly) and different instruments (MC-ICP-MS vs. IRMS), the vast majority of samples agree to within 10% or better, with a difference generally <±0.2‰ (2 s.d.; except for two samples with 0.3‰ (2 s.d.); see Table S2 and Figure S1). The good agreement between the two laboratories is further illustrated by the random distribution of samples and standards from both laboratories along a 1:1 line (Figure 2), which eliminates the possibility of a systematic bias in the determined Si isotope composition. Although some interlaboratory comparisons have observed a constant offset between their δ^{30}Si measurements (see Brzezinski & Jones, 2015), our observations confirm the previously published conclusion that there is no systematic offset between MC-ICP-MS and IRMS (B. C. Reynolds et al., 2007; Grasse et al., 2017).

External reproducibility (2 s.d.) of reference materials analyzed in the two laboratories ranges between 0.1‰ to 0.3‰ and 0.2‰ to 0.3‰ for GEOMAR and UCSB, respectively. These results are similar to those obtained during the interlaboratory comparison of Si isotopes in seawater (Grasse et al., 2017) and in pure solid siliceous materials (B. C. Reynolds et al., 2007). The mean results for all reference materials δ^{30}Si were in very good agreement (<±0.1‰ difference) except for $ALOHA_{300}$ (0.36‰ difference, Table S3), which is similar to the 0.32‰ difference observed between the two laboratories during the interlaboratory comparison. In their interlaboratory comparison exercise, Grasse et al. (2017) previously pointed out a better reproducibility for $ALOHA_{1000}$ compared to $ALOHA_{300}$ (±0.2‰ vs. ±0.4‰, 2 s.d.) among and within laboratories. They suggest that possible origin of the larger variance of measurements for $ALOHA_{300}$ could be the occurrence of seawater ions that are not removed during purification using the cation exchange resins or the higher DOC to Si ratio in the shallow sample. Any element remaining in the final solution can compete with Si for ionization during analysis, especially when using MC-ICP-MS, and thus can potentially induce a matrix effect and bias the final δ^{30}Si.

The isotope fractionation for Si is mass dependent resulting in a linear relationship between δ^{30}Si and δ^{29}Si that depends on the fractionation process (equilibrium vs. kinetic fractionation). The slope of the resulting correlation is thus an indicator for the quality of δ^{30}Si measurements, as any polyatomic interference during MC-ICP-MS measurements or the presence of interfering masses for IRMS measurement would lead to an offset from the predicted fractionation line. As shown in Figure S2, the least squares linear regression between δ^{30}Si and δ^{29}Si is in excellent agreement for both laboratories and produces a slope of 0.509 ± 0.001 ($R^2 = 0.99$), which is not distinguishable from the theoretical values of equilibrium and kinetic fractionations (0.518 and 0.505, respectively; Young et al., 2002). This confirms the absence of isobaric interference problems during isotopic analysis in both laboratories.

3.2. [DSi] and δ^{30}Si Distribution Along GP16

Surface waters (approximately upper 200 m) display the commonly observed inverse relationship between δ^{30}Si and [DSi] with the heaviest δ^{30}Si values associated to low [DSi] surface waters (Figures 1b and 3). [DSi] in surface waters ranged from 1 to 5 μmol kg^{-1} with the highest concentrations at Station 7 and Station 9 in proximity to Peru. Here, the lightest δ^{30}Si (+2.3‰ to +2.5‰) in surface waters is observed (Figure 3 and Table S1). Surface waters west of 100°W longitude have the lowest [DSi] (1 to 2 μmol kg^{-1}) accompanied by heavy δ^{30}Si (up to +3.5‰). A strong decrease in [NO_3^-] is also observed west of 100°W (Figure S3). Most of the longitudinal variation in δ^{30}Si across the GP16 transect is limited to the

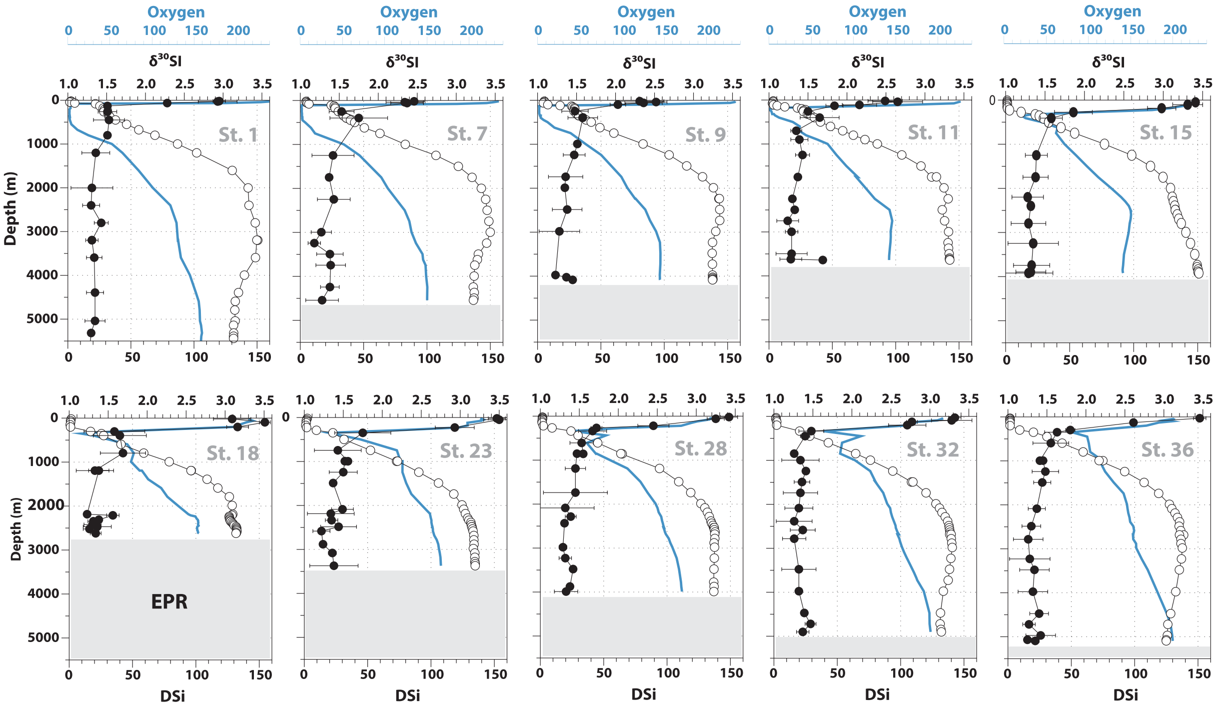

Figure 3. Depth profiles along the GP16 transect showing δ^{30}Si in ‰ (black dots) and [DSi] in μmol kg^{-1} (open black symbols) together with the oxygen concentration in μmol kg^{-1} (blue line). The gray-shaded area indicates the bottom depth including the location of the East Pacific Rise (EPR, Station 18). Error bars represent the individual 2 s.d. of each sample.

oxygenated upper water column (Figure 3). Below, δ^{30}Si at all stations decreases sharply to approximately +1.6‰ associated with a strong increase in [DSi], which is closely linked to the upper oxycline (Figure 3). In close proximity to Peru (Stations 1, 7, 9, and 11) a strong OMZ is observed with oxygen concentrations close to zero that lies within a potential density (σ_θ) range of 26.2 to 27.0 kg m^{-3} (Figure 3 and Table S1). West of 100°W oxygen concentrations within the oxygen minimum slowly begin to increase with the highest oxygen concentrations (110 μmol kg^{-1}) at Stations 23 and 36 (300 m; Figures 3 and S4). Despite the large range in oxygen concentrations as well as in [DSi] (from 10 to 40 μmol kg^{-1}), no clear shift in δ^{30}Si between σ_θ of 26.2 to 27.0 kg m^{-3} is observed (+1.6 ± 0.1‰; mean ± 1 s.d.; Figure S4).

At most stations (Stations 1, 7, 9, 32, and 36) [DSi] increases with depth to a maximum concentration (up to 150 μmol kg^{-1}) between 2,000 and 4,000 m. Below, [DSi] either decreases by up to 15% (Stations 1,7, 9, 32, and 36), stays constant (Stations 11, 18, 23, and 28), or shows an increase toward the bottom (Station 15). However, these changes in [DSi] are not reflected in the corresponding δ^{30}Si values, which remain rather constant below 1,000 m with a mean of +1.4 ± 0.1‰ (1 s.d.) ranging from +1.2‰ to +1.6‰ excluding one suspicious value of +1.69‰ at Station 11 (3,640 m). Below 2,000 m the average δ^{30}Si is +1.3 ± 0.1‰ (1 s.d.).

The station located nearly directly above the EPR (Station 18) shows a slightly different [DSi] distribution. Here, [DSi] increases until 2,000 m to 130 μmol kg^{-1}, the lowest concentration at this depth compared to all other stations, and then [DSi] slightly decreases (125 μmol kg^{-1}). At 2,500 m [DSi] increases again to (132 μmol kg^{-1}). δ^{30}Si above the EPR (2,211 to 2,620 m) is rather constant around +1.4 ± 0.1‰ (mean, 1 s.d.), except for the sample at 2,211 m, where δ^{30}Si is enriched (+1.6 ± 0.1‰, 2 s.d.).

4. Discussion

4.1. Controls on the δ^{30}Si Distribution in Surface and Subsurface Waters

The observed trend between low [DSi] and high δ^{30}Si values in surface waters is generally attributed to the fractionation of Si during DSi consumption by siliceous phytoplankton (De La Rocha et al., 1997; J. Sutton et al., 2018). Whereas in coastal upwelling systems diatoms dominate the phytoplankton community, further offshore generally nonsiliceous phytoplankton, such as the cyanobacteria *Synechococcus* and *Prochlorococcus*

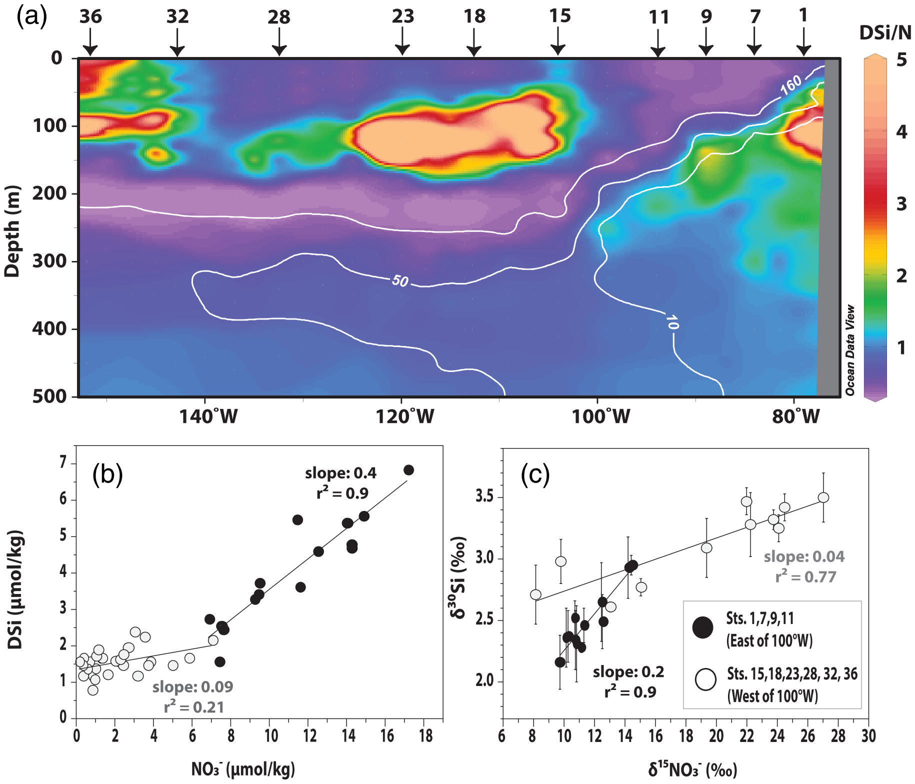

Figure 4. (a) DSi/NO_3^- (DSi/N) ratios in the upper 500 m including oxygen contour lines (white). (b) DSi versus NO_3^- as well as (c) δ^{30}Si versus $\delta^{15}NO_3^-$ in the upper oxygenated water column (oxygen >160 µmol kg^{-1}; depth <200 m). δ^{15} NO_3^- data are adapted from Peters, Lam, and Casciotti (2018).

are observed (e.g., Estrada & Blasco, 1985; Franz et al., 2012). The strong influence of siliceous phytoplankton, most likely diatoms at stations east of 100°W, is illustrated by the ratio between DSi to NO_3^- (DSi/N) that indicates utilization of 0.4 mol of DSi for each mole of NO_3^-, whereas west of 100°W longitude, the slope declines to 0.1 mol DSi per NO_3^- (Figures 4a and 4b). The relative utilization of DSi and N is also reflected in the strong correlation between δ^{30}Si and the stable isotope composition of NO_3^- ($\delta^{15}NO_3^-$, adapted from Peters, Lam, & Casciotti, 2018; Figure 4c). DSi/N ratios, observed during GP16, are comparable to a study by Grasse et al. (2016), where in close proximity to Peru DSi/N ratios of 0.5 were observed, which decreased in offshore waters to 0.1 mol of DSi for each mole of NO_3^-. Diatoms normally incorporate DSi and N at a 1:1 mole ratio (Brzezinski, 1985; Ragueneau et al., 2000), but stress, such as Fe limitation, can lead to an enhanced uptake of DSi over N resulting in heavier silicified frustules of the diatoms (Hutchins & Bruland, 1998; Franck et al., 2003). During the EPZT dissolved Fe (dFe) and other trace metals, like zinc (Zn) and Cadmium (Cd), were never completely depleted in upper 50 m of the eastern transect (up to 0.1 to 0.2 nmol; S. G. John et al., 2018, Figure S3). Thus, changes in the DSi/N consumption ratio and the shift in the slope of the relationship between δ^{30}Si and ($\delta^{15}NO_3^-$) likely reflect the enhanced prevalence of non-siliceous organisms from coast to gyre waters (Conley & Malone, 1992; Wilkerson & Dugdale, 1996).

Besides DSi utilization, the δ^{30}Si signal in surface waters is strongly influenced by upwelling intensity and by horizontal mixing by eddies (Ehlert et al., 2012; Grasse et al., 2013, 2016). During strong upwelling along the Peruvian coast, surface waters are supplied with DSi-rich subsurface waters (e.g., Bruland et al., 2005). Subsurface waters in proximity to the Peruvian coast are composed of ESSW, a coastal water mass that is transported southwards along the Peruvian coast with the Peru Chile Undercurrent (e.g., Montes et al., 2010; Thomsen et al., 2016). ESSW is typically characterized by very low N:P as well as high DSi/N ratios, due to the removal of NO_3^- via denitrification and/or annamox in anoxic coastal waters off Peru (Figure 4; Codispoti, 2007; Franz et al., 2012; Grasse et al., 2016; Kalvelage et al., 2013; Silva et al., 2009). Additionally, [DSi] in coastal areas is elevated due to high remineralization rates as well as benthic fluxes from the sediments (Ehlert et al., 2016; Grasse et al., 2016). Along the Peruvian coast [DSi] up to

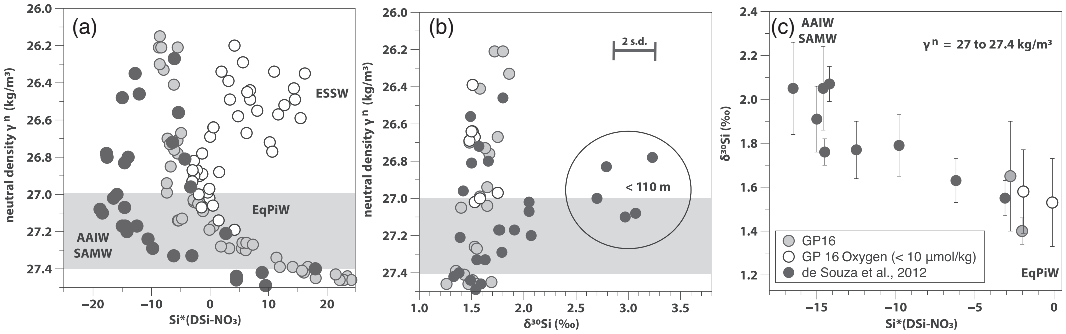

Figure 5. Neutral density γ^n (kg m^{-3}) versus (a) Si* (Si* = [DSi] − [NO_3^-]; Sarmiento et al. (2004) and (b) δ^{30}Si, for subsurface (ESSW) as well as intermediate water masses (AAIW/SAMW and EqPIW) for comparison between data obtained during a transect along 103°W in the eastern South Pacific (de Souza, Reynolds, Johnson, et al., 2012, black dots) and the GP16 data (gray dots and open symbols). Samples along GP16 with oxygen concentrations less than 10 μmol kg^{-1} are indicated by open symbols. A negative Si* (−20 μmol kg^{-1}) indicates subducted surface water masses from the Southern Ocean (AAIW/SAMW; de Souza, Reynolds, Johnson, et al., 2012), whereas a positive Si* (+20 μmol kg^{-1}) is typically found in low oxygen coastal waters (ESSW; <10 μmol kg^{-1}). According to Peters, Jenkins, et al. (2018), the EqPIW is defined by Si* of approximately 0 μmol kg^{-1}. The gray-shaded area indicates intermediate waters within a density range (γ^n) of 27 to 27.4 kg m^{-3}, which are plotted in (c) showing the decrease in δ^{30}Si coupled to an increase in Si* between AAIW/SAMW and EqPIW.

40 μmol kg^{-1} in subsurface waters has been observed with an average δ^{30}Si of +1.5 ± 0.2‰ (1 s.d.; Ehlert et al., 2012) similar to our observations at Station 1 (Figure 3). Very recent upwelling can therefore lead to δ^{30}Si signals in surface waters as low as +1.7‰, when only 50% of the available [DSi] pool is utilized (Ehlert et al., 2012). In contrast, surface waters west of 100°W show the highest δ^{30}Si values (up to +3.5‰; 2 μmol kg^{-1}) due to a high utilization of the available [DSi] pool (Figure 3). However, the [DSi] pool is never completely exhausted, possibly due to NO_3^- limitation ([NO_3^-] < 1 μmol kg^{-1}) resulting in very high DSi/N ratios (~4) at the most western part of the transect (Figure 4a). Potential colimitation with Fe, zinc (Zn), or cadmium (Cd) cannot be excluded, even though none of the micronutrients are completely exhausted in the upper 50 m (D. G. John et al., 2017; S. G. John et al., 2018; Figure S3).

Subsurface waters (σ_θ: 26 to 27 kg m^{-3}) further offshore are mainly dominated by Eastern South Pacific Intermediate Water (ESPIW, up to 60%, Station 15) and South Pacific Central Water (SPCW, up to 45%, Station 36). Compared to ESSW, which generally has oxygen concentrations below 10 μmol kg^{-1}, ESPIW and SPCW are well oxygenated (50 to 110 μmol kg^{-1}, Figures 1b, 3, and 5a). Interestingly, the subsurface waters show no significant variation in δ^{30}Si (+1.6 ± 0.1‰; mean ± s.d.; Figure S4) despite a 30 μmol kg^{-1} difference in [DSi] across the complete section from Peru to Tahiti (Figure 3). However, a strong coupling between the upper oxycline and the sudden increase in [DSi] and decrease in δ^{30}Si can be observed, showing that the oxycline represents the shift from well-ventilated waters to poorly ventilated, old waters of the OMZ.

4.2. Intermediate Water δ^{30}Si Values

Intermediate waters (neutral density γ^n: 27 to 27.4 kg m^{-3}) are mainly characterized by a mixture of AAIW, Subantarctic Mode Water (SAMW), and EqPIW. Whereas EqPIW reflects a rather "old" water mass, enriched in [DSi] (Bostock et al., 2013), AAIW and SAMW are relatively "young" subducted surface water masses from the Southern Ocean, depleted in [DSi] (e.g., Sarmiento et al., 2004). This is reflected in their DSi concentrations and in their δ^{30}Si values. A study by de Souza et al. (2012) was able to track AAIW/SAMW, using its negative Si* (~ −20 μmol kg^{-1}; Sarmiento et al., 2004) and its original high δ^{30}Si signature at high southern latitudes (up to +1.8 to +2‰ below the mixed layer and up to +3.2‰ within the mixed layer; Figure 5b) to approximately 20°S. Toward the north δ^{30}Si is decreasing due to admixture with EQPIW, water masses from the north (Figure 5c). EqPIW prevails, north of 20°S with elevated [DSi], visible by a positive Si* (+23 μmol kg^{-1}) as well as lower δ^{30}Si (Figures 5a and 5c). According to the OMPA analysis of Peters, Jenkins, et al. (2018), Station 18 (800 m) has the highest contribution of AAIW (50%) and already shows a positive Si* (18 μmol kg^{-1}) and only a slightly elevated δ^{30}Si of +1.7 ± 0.3‰. Given that the AAIW end-member has a relatively low DSi concentration (13 μmol kg^{-1}, Peters, Jenkins, et al., 2018), its contribution to the [DSi] at this station is only 11%, consistent with the lack of a significant influence of AAIW on δ^{30}Si at this latitude (10°S to 15°S). In contrast to AAIW/SAMW, EqPIW in equatorial regions show δ^{30}Si values of approximately +1.5‰ (Beucher et al., 2008; Grasse et al., 2013), which agrees well with Stations 28 and 36 (~600 m, +1.53 ± 0.15‰ and 1.55 ± 0.23‰, respectively) where we see the highest attribution of EqPIW (70% to 80%). Considering the external reproducibility of the δ^{30}Si measurement of 0.2‰, intermediate waters show little variation in δ^{30}Si (overall mean of +1.5 ± 0.1‰) across the transect indicating that mixing and other processes have erased the original positive δ^{30}Si signatures of AAIW and SAMW (Figure 5c).

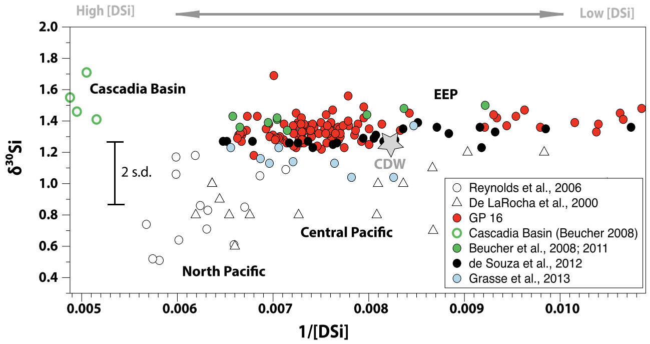

Figure 6. Comparison of published δ^{30}Si data from the deep Pacific (>1,000 m) Grasse et al. (2013; blue dots), de Souza, Reynolds, Johnson, et al. (2012; black dots), Beucher et al. (2008, 2011; green dots), and the GP16 transect (red dots). Besides a homogenous δ^{30}Si along the ETSP as well as the southern Pacific, some Central Pacific (open triangles; De La Rocha et al., 2000) samples as well as North Pacific samples show very light δ^{30}Si values (open circles; B. Reynolds et al., 2006), which contrasts with isotopically heavy values from the Cascadia Basin (Jones, personal communication, 17.05.2019; Beucher et al., 2008). A Southern Ocean end-member (CDW) is indicated with a gray star (de Souza, Reynolds, Johnson, et al., 2012; de Souza, Reynolds, Rickli, & Frank, 2012; Orsi et al., 1999). The error bar (2 s.d. = 0.2‰) corresponds to the external reproducibility reported for the ALOHA_{1000} intercalibration standard.

4.3. Deep Water δ^{30}Si Values

Deep waters between 1,500 and 3,000 m ($27.5 < \sigma_\theta < 27.73$) are dominated by Upper Circumpolar Deep Water (UCDW) and PDW. PDW is one of the oldest water masses in the global ocean and most likely formed through upwelling and diapycnal diffusion of northward-flowing bottom waters (Talley, 2008). It is characterized by [DSi] of up to 170 μmol kg^{-1} and can be distinguished from UCDW, which has higher oxygen concentrations and lower DSi concentrations (77 μmol kg^{-1}; see references in Peters, Jenkins, et al., 2018). UCDW is mainly present west of 100°W between 1,000 and 3,000 m with contribution ranging from 40% to 60%, whereas PDW dominates around 80°W to 100°W (Figure 1b). Only small differences in δ^{30}Si have been observed between UCDW and LCDW (on average +1.3 ± 0.1‰ and +1.0 ± 0.1‰; Closset et al., 2016). In the present data set these differences were not apparent with δ^{30}Si of deep water masses (below 2,000 m) averaging +1.3 ± 0.1‰.

The densest water masses in the region are AABW and Lower Circumpolar Deep Water (LCDW) (Peters, Jenkins, et al., 2018; Figure 1b). These water masses have similar NO_3^-, PO_4^- but different [DSi] end-member concentrations with lower [DSi] (92 μmol kg^{-1}) for LCDW and higher [DSi] (144 μmol kg^{-1}) for AABW. After leaving the Southern Ocean these water masses encounter admixture with other deep water masses (e.g., North Pacific Deep Water [NPDW]) during transit through the Pacific Basin (Kawabe & Fujio, 2010). Previous work in the Southern Ocean (Drake Passage, South of Australia, Indo-Atlantic) has shown that the main water mass, CDW, has a relatively homogenous δ^{30}Si of +1.2‰ (Cardinal et al., 2005; de Souza, Reynolds, Johnson, et al., 2012; de Souza et al., 2012), which is indistinguishable from AABW (Brzezinski & Jones, 2015; de Souza et al., 2014; de Souza, Reynolds, Rickli, & Frank, 2012; Holzer & Brzezinski, 2015).

According to the OMPA analysis of Peters, Jenkins, et al. (2018), AABW contribution exceeds 40% in the western part of the transect, associated to higher oxygen concentrations (>175 μmol kg^{-1}) and <20% east of EPR associated to oxygen concentrations around 150 μmol kg^{-1}. Stations with the strongest attribution of LCDW (50%; Station 1) and AABW (52%; Station 36) do not show distinct δ^{30}Si values (+1.3‰ and +1.3‰, respectively) (Figures 3 and 4) contributing to a remarkable homogeneity for deep water δ^{30}Si in this region of the Pacific.

The averaged deep water (>2,000 m) δ^{30}Si (+1.3 ± 0.1‰) is in excellent agreement with +1.3‰ and 1.4‰ reported by Beucher et al. (2008, 2011) for the deep equatorial Pacific and with previously published values reported by de Souza, Reynolds, Johnson, et al. (2012) covering a transect from the Southern Ocean up to 10°S. Grasse et al. (2013) show slightly lighter δ^{30}Si of +1.2‰, which is however within external precision (Figures 6 and S5). A high level of homogeneity in the deep Pacific is predicted by models (e.g., B. C. Reynolds, 2009; de Souza et al., 2014; Gao et al., 2016; Wischmeyer et al., 2003). Both numerical models and observations show that globally δ^{30}Si declines nearly logarithmically with increasing [DSi] such that δ^{30}Si becomes nearly invariant (relative to measurement error) for [DSi] > ~100 μM. This leads to an expected isotopic homogeneity of δ^{30}Si between +1.1‰ and +1.2‰, for the entire deep Pacific given the high [DSi] found throughout the deep portions of the basin. Our data from the Southeast Pacific are consistent with this prediction. However, some extremely low (North Pacific) and relatively high (Cascadia Basin)

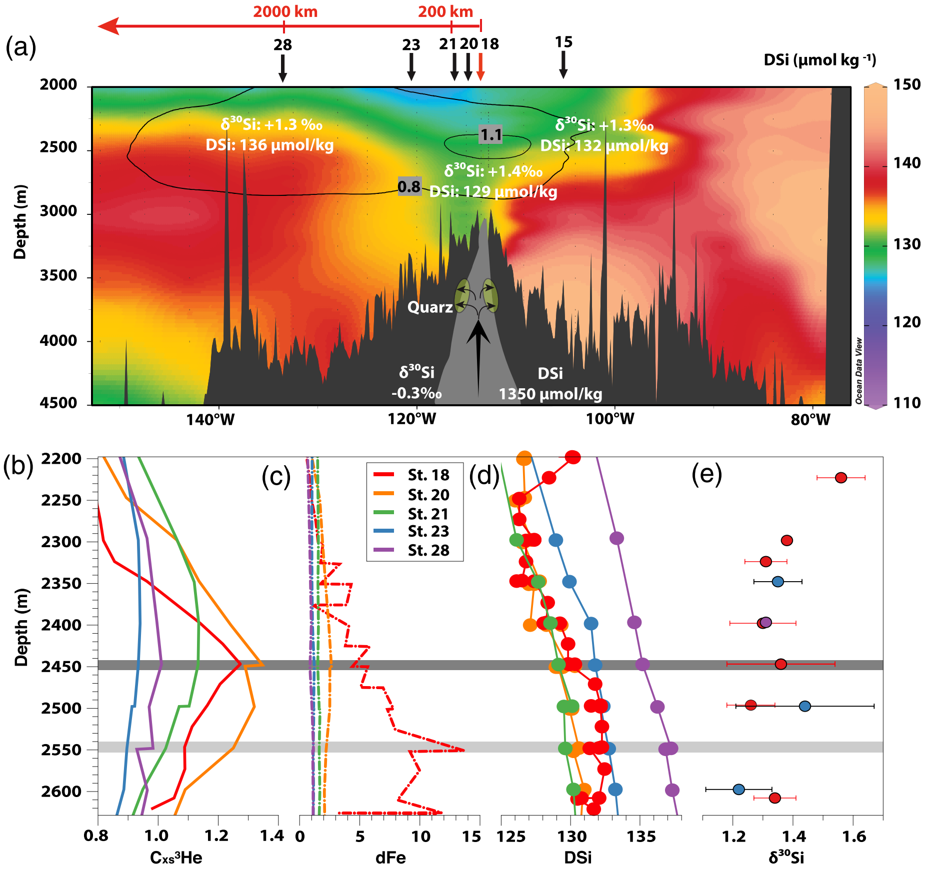

Figure 7. (a) Schematic figure of the GP16 transect below 2,000 m. The plume can be identified at Station 18 (and further west) by increased excess ^{3}He ($C_{ex}{}^{3}$He in fmol kg^{-1}; density lines) relative to surrounding waters with maximum concentrations centering at 2,450 m depth (Jenkins et al., 2018; Resing et al., 2015). [DSi] and δ^{30}Si reported in (a) represent mean values between 2,200 and 2,600 m for Station 15 (132 µmol kg^{-1}; 1.3‰), Stations 18, 20, and 21 (129 µmol kg^{-1}, +1.4‰), Station 23 (132 µmol kg^{-1}; +1.4‰; not shown), and Station 28 (136 µmol kg^{-1}; +1.3‰). (b–e) Selected stations above and west of the EPR with (b) $C_{ex}{}^{3}$He (fmol kg^{-1}), (c) dFe (nmol kg^{-1}), (d) DSi (µmol kg^{-1}), and (d) δ^{30}Si versus depth (m). δ^{30}Si is only available from Stations 18 and 23 and one data point at Station 28. The dark gray area indicates the depth of the $C_{ex}{}^{3}$He peak (2,450 m) and the light gray area the maximum [dFe] (2,550 m). Please note, that dFe data is sampled on a diffrent cast than the [DSi] and $C_{ex}{}^{3}$He data. Small differences in peak concentrations for [dFe] and [DSi] are most likely due to natural variability of the plume.

δ^{30}Si signatures have been measured in other areas of the deep Pacific (Figure 5) presenting what de Souza, Reynolds, Johnson, et al. (2012) referred to as the deep Pacific "conundrum" due to their strong deviation from model predictions. The reasons given so far to explain the unexpected variability in δ^{30}Si across the deep Pacific are measurement inaccuracies with older δ^{30}Si data, especially for the North West Pacific (de Souza, Reynolds, Johnson, et al., 2012) or additional sources, such as the Northeast Pacific DSi Plume, which have not been considered in modeling attempts (Hendry & Brzezinski, 2014).

4.4. Influence of the EPR on Deep δ^{30}Si

The hydrothermal plume emanating from the EPR provides us the opportunity to evaluate the impact of hydrothermal activity on [DSi] and δ^{30}Si distributions in the deep Pacific. The plume can be identified at Station 18 by increased excess ^{3}He ($C_{ex}{}^{3}$He) relative to surrounding waters, which is then transported laterally more than 4,000 km westward at depths between 2,000 and 3,000 m (Figure 7; Resing et al., 2015; Jenkins et al., 2018).

The influence of hydrothermal inputs on the global marine Si cycle remains uncertain due to the paucity of δ^{30}Si data from the source and only limited data sets close to deep vents (Brzezinski & Jones, 2015; De La Rocha et al., 2000; Liguori et al., 2020). To date, the only published data for originally hot hydrothermal

Table 1
Potential Source Water Contributions of the Main Water Masses in the Region (PDW, UCDW, and LCDW) and Their Impact on [DSi] Variation in Plume Waters (Station 18, >2,200 m, 129 μmol kg^{-1})

PDW	UCDW	LCDW	Calculated δ^{30}Si	Calculated DSi	DSi enriched/ depleted
%	%	%	‰	μmol kg^{-1}	%
50	25	25	1.20	125.25	3
60	20	20	1.20	133.40	−3
70	15	15	1.20	141.55	−10
80	10	10	1.20	149.70	−16
90	5	5	1.20	157.85	−22
100	0	0	1.20	166.00	−29

Note. According to OMPA calculations by Peters, Jenkins, et al. (2018), the PDW contribution within the plume was 60 ± 10%. End-member concentrations according to Peters, Jenkins, et al. (2018) were 166 μmol kg^{-1} for PDW, 77 μmol kg^{-1} for UCDW, and 92 μmol kg^{-1} for LCDW.

fluids (~300°C) were sampled from the EPR at 9°N (−0.4‰ and −0.2‰; De La Rocha et al., 2000), which reflects δ^{30}Si of the earth mantle (−0.3 ± 0.1‰, 2 s.d.; Douthitt, 1982; Savage et al., 2010). Due to extremely high [DSi] (13,550 μmol kg^{-1}) in these fluids and the low δ^{30}Si of the hydrothermal end-member, hydrothermal influence is generally considered as a source for [DSi] (De La Rocha et al., 2000; J. Sutton et al., 2018).

Interestingly, hydrothermal plume waters (Stations 18, 20, and 21 ≥2,200 m) are significantly lower in [DSi] (129 μmol kg^{-1}) compared to hydrothermal fluids and, therefore, within a similar range or even slightly less concentrated compared to waters adjacent to the main plume (Figures 7 and S6). We only observed a minimal increase in [DSi] (~3 μmol kg^{-1}) compared to shallower and deeper waters, together with an increase in [dFe]. Maximum concentrations in [DSi] and dFe are slightly below the maximum $C_{ex}{}^{3}$He concentration (centered at 2,450 m) (Figures 7c, 7d, and S6). Large amounts of hydrothermal Si do not reach the Pacific deep water and must, therefore, precipitate within the conduit and/or at the rim of the vent. Amorphous silica precipitates rapidly during fluid ascent in the conduit either as amorphous silica, quartz, or further secondary mineral upon conductive cooling of hydrothermal solutions with seawater (Elderfield & Schultz, 1996; Mortlock et al., 1993). This is further supported by the findings of Feely et al. (1990). They found a general decrease in grain size of precipitated amorphous silica particles with increasing distance to vents in the Juan de Fuca Ridge. They suspected that most of the Si loss occurs within or very close to the vent. In addition, a study by Lam et al. (2018) observed a very small enhancement in “biogenic Si” (most likely amorphous silica) at station 18, a possibly hint, that DSi is converted into a solid phase. The precipitation of [DSi] as quartz is associated with a fractionation, where light isotopes are preferentially incorporated into the solid phase, whereas the fluid phase can be enriched in ^{30}Si (Geilert et al., 2015; Kleine et al., 2018). Additionally, DSi shows a strong adsorption affinity to Fe(III) oxyhydroxides (Davis et al., 2002; Feely et al., 1994), which form, when hydrothermal fluid gets into contact with oxygenated seawater. This process is known to induce a Si isotope fractionation of approximately −1‰ (Delstanche et al., 2009). The precipitation of DSi causes an increase in δ^{30}Si within the conduit such that hydrothermal fluids reaching the rim do not differ significantly from seawater δ^{30}Si (Figure 7a).

Despite the minimal increase in [DSi] (~3 μmol kg^{-1}) at approximately 2,550 m, stations close to the EPR (Stations 18, 20, and 21) are generally depleted in [DSi] compared to Stations 23 and 28 further west (~3 to 6 μmol kg^{-1}). Previous studies along the EPR have speculated that the hydrothermal plume might not be a continuous “smoke plume” emanating from a single location on the EPR (Jenkins et al., 2018) and that the higher $C_{ex}{}^{3}$He concentration further west (Station 20, Figure 7a) might be influenced from vent fields located further south (17°S–18.5°S) on the EPR (Resing et al., 2015, and references therein). Therefore, the estimation of the hydrothermal share in deep seawater is rather difficult due to poorly constrained end-members. Whereas seawater end-member [DSi] can potentially be estimated from observations along the GP16 transect, [DSi] in hydrothermal fluids was not measured during GP16, and the only estimates are from the EPR around 9°N, with potentially different vent fluid dynamics. Rough estimates taking a 2 to 3 μmol kg^{-1} increase into account would result in a meager hydrothermal share (0.02%) considering a high [DSi] of 14 mmol kg^{-1} for the hydrothermal fluid (De La Rocha et al., 2000). However, such hydrothermal share calculations do not take abiotic processes into account, such as the formation of Fe(III) oxyhydroxides in the water column (Fitzsimmons et al., 2017) and the potential adsorption of DSi onto those particles.

In another approach we estimated the enrichment/depletion of hydrothermal plume waters (Station 18, >2,200 m, 129 μmol kg^{-1}) to surrounding seawater. According to the OMPA analysis by Peters, Jenkins, et al. (2018), water masses above the EPR consist of PDW (60 ± 10%), UCDW (20 ± 10%), and LCDW (20 ± 10%). Even though Peters, Jenkins, et al. (2018) assumed that the bottom waters were not dramatically altered by the hydrothermal plume, as key parameters (e.g., temperature, salinity, and [DSi]) did not change significantly, small changes in [DSi] might not have been taken into account. We therefore calculated a potential background [DSi] using different fractions of PDW (Table 1), which has the highest [DSi]

(166 μmol kg^{-1}) and thus will display the highest sensitivity to any hydrothermal dilution. For example, with 50% contribution of PDW, the expected [DSi] of the seawater with no hydrothermal share ($\delta^{30}Si = +1.2‰$) is 125.25 μmol kg^{-1} instead of the 129 μmol kg^{-1} measured in the plume at Station 18. Depending on the source water, the EPR could ultimately serve as a source or a sink for [DSi]. Whereas an enrichment (up to 3%) most likely would result from hydrothermal input and/or water mass mixing, a depletion (up to 10%) could result from direct DSi precipitation as, that is, quartz or by scavenging of Si by Fe(III) oxyhydroxide particles within plume waters (e.g., Davis et al., 2002; Elderfield & Schultz, 1996; Feely et al., 1994; Mortlock et al., 1993).

However, given the small differences in [DSi], it is difficult to make robust estimates and disentangle water mass mixing and abiotic processes. Overall, the influence of hydrothermal fluids on the [DSi] and δ^{30}Si in deep waters seems to be negligible, which is in accordance to studies in the North Atlantic (Brzezinski & Jones, 2015) and Arctic (Liguori et al., 2020) oceans, where no apparent effect on the δ^{30}Si in deep waters was detected.

5. Conclusions

In this study, we present δ^{30}Si data from the GEOTRACES GP16 transect from Peru to Tahiti. δ^{30}Si was measured at two laboratories (GEOMAR and UCSB), and intercalibration between samples with high and low [DSi] resulted in excellent agreement (generally <0.2‰; 2 s.d.).

The results show a strong gradient in surface water δ^{30}Si values with moderately fractionated waters in the vicinity to Peru and highly fractionated surface waters in the subtropical gyre. A strong coupling between the upper oxycline and the sudden increase in [DSi] and a decrease in δ^{30}Si was observed. However, δ^{30}Si values did not differ between samples within the OMZ and at higher oxygen concentrations (>50 μmol O_2 kg^{-1}) at similar water density. Overall, δ^{30}Si below 2,000 m showed a homogenous distribution, despite the relatively broad range in [DSi] (up to 25 μmol kg^{-1}) and the presence of water masses with both northern and southern origin. The uniformity in δ^{30}Si is in very good agreement to previously published data in the region and matches the predictions from models that δ^{30}Si should be invariant relative to measurement error (±0.2‰) for [DSi] > ~100 μmol kg^{-1}.

We observe very little input and perhaps even a small reduction of [DSi] in bottom waters close to the EPR. A large fraction of [DSi] must therefore already precipitate within the conduit of the EPR. Additionally, Fe(III) particles in the water column might scavenge DSi. However, given the small differences in [DSi] and no measurable effect on δ^{30}Si, hydrothermal fluids seem to have a neglectable impact on the deep Si cycle.

The present study significantly expands the δ^{30}Si data set for the Pacific and confirms past observations and models that suggest a homogenous δ^{30}Si distribution below 1,000 m in this region. This high degree of homogeneity is at odds with measurements in the North Pacific that show values that are both higher and lower than expectations. Additional transects with expanded spatial coverage, especially in the Northwest Pacific and the Cascadia Basin, will be necessary to resolve the apparent basin-scale variability.

Data Availability Statement

Additional data from the U.S. GEOTRACES EPZT (GP 16) were published in a special issue edited by James Moffett in 2018 (Marine Chemistry, Volume 201, pp. 1–262). δ^{30}Si data are available through the Biological and Chemical Oceanography Data Management Office Website (https://www.bco-dmo.org/dataset/728819).

Acknowledgments

We greatly thank Captain Russ DeVaney and the crew of the *R/V* Thomas G. Thompson, as well as the Chief Scientists Jim Moffett and Chris German, for a successful cruise. This work was made possible by funding from the National Science Foundation (NSF) OCE-1233028 as well as funding from the funding by the Collaborative Research Centre 754 "Climate-Biogeochemistry Interactions in the Tropical Ocean" (www.sfb754.de), supported by the Deutsche Forschungsgemeinschaft (DFG; SFB 754).

References

Atlas, E. L., Hager, S. W., Gordon, L. I., Park, P. K. (1971). A practical manual for use of the Technicon AutoAnalyzer® in seawater nutrient analyses revised. Technical Report 215, Reference 71-22. Oregon State University, Department of Oceanography, pp. 49.

Beucher, C. P., Brzezinski, M. A., & Jones, J. L. (2008). Sources and biological fractionation of Silicon isotopes in the Eastern Equatorial Pacific. *Geochimica et Cosmochimica Acta*, *72*(13), 3063–3073. https://doi.org/10.1016/j.gca.2008.04.021

Beucher, C. P., Brzezinski, M. A., & Jones, J. L. (2011). Mechanisms controlling silicon isotope distribution in the Eastern Equatorial Pacific. *Geochimica et Cosmochimica Acta*, *75*(15), 4286–4294. https://doi.org/10.1016/j.gca.2011.05.024

Bostock, H. C., Sutton, P. J., Williams, M. J., & Opdyke, B. N. (2013). Reviewing the circulation and mixing of Antarctic Intermediate Water in the South Pacific using evidence from geochemical tracers and Argo float trajectories. *Deep Sea Research Part I: Oceanographic Research Papers*, *73*, 84–98. https://doi.org/10.1016/j.dsr.2012.11.007

Bruland, K. W., Rue, E. L., Smith, G. J., & DiTullio, G. R. (2005). Iron, macronutrient and diatom blooms in the Peru upwelling regime: Brown and blue waters of Peru. *Marine Chemistry*, *93*(2-4), 81–103. https://doi.org/10.1016/j.marchem.2004.06.011

Brzezinski, M. A. (1985). The Si:C:N ratio of marine diatoms: Interspecific variability and the effect of some environmental variables[1]. *Journal of Phycology*, *21*(3), 347–357.

Brzezinski, M. A., & Jones, J. L. (2015). Coupling of the distribution of silicon isotopes to the meridional overturning circulation of the North Atlantic Ocean. *Deep Sea Research Part II: Topical Studies in Oceanography*, *116*, 79–88. https://doi.org/10.1016/j.dsr2.2014.11.015

Brzezinski, M. A., Jones, J. L., Bidle, K., & Azam, F. (2003). The balance between silica production and silica dissolution in the sea: Insights from Monterey Bay, California, applied to the global data set. *Limnology and Oceanograpy*, *48*(5), 1846–1854. https://doi.org/10.4319/lo.2003.48.5.1846

Brzezinski, M. A., Jones, J. L. J., Beucher, C. P. C., Demarest, M. S. M., & Berg, H. L. H. (2006). Automated determination of silicon isotope natural abundance by the acid decomposition of cesium hexafluosilicate. *Analytical Chemistry*, *78*(17), 6109–6114. https://doi.org/10.1021/ac0606406

Cardinal, D., Alleman, L. Y., Dehairs, F., Savoye, N., Trull, T. W., & André, L. (2005). Relevance of silicon isotopes to Si-nutrient utilization and Si-source assessment in Antarctic waters. *Global Biogeochemical Cycles*, *19*, GB2007. https://doi.org/10.1029/2004GB002364

Closset, I., Cardinal, D., Rembauville, M., Thil, F., & Blain, S. (2016). Unveiling the Si cycle using isotopes in an iron-fertilized zone of the Southern Ocean: From mixed-layer supply to export. *Biogeosciences*, *13*(21), 6049–6066. https://doi.org/10.5194/bg-13-6049-2016

Codispoti, L. A. (2007). An oceanic fixed nitrogen sink exceeding 400 Tg N a^{-1} vs the concept of homeostasis in the fixed-nitrogen inventory. *Biogeosciences*, *4*, 233–253. https://doi.org/10.5194/bg-4-233-2007

Conley, D. J., & Malone, T. C. (1992). Annual cycle of dissolved silicate in Chesapeake Bay: Implications for the production and fate of phytoplankton biomass. *Marine Ecology Progress Series. Oldendorf*, *81*(2), 121–128. https://doi.org/10.3354/meps081121

Davis, C., Chen, H., & Edwards, M. (2002). Modeling silica sorption to iron hydroxide. *Environmental Science & Technology*, *36*(4), 582–587. https://doi.org/10.1021/es010996t

De La Rocha, C. L., Brzezinski, M. A., & DeNiro, M. J. (1996). Purification, Recovery, and Laser-Driven Fluorination of Silicon from Dissolved and Particulate Silica for the Measurement of Natural Stable Isotope Abundances. *Analytical Chemistry*, *68*(21), 3746–3750. https://doi.org/10.1021/ac960326j

De La Rocha, C., Brzezinski, M. A., & DeNiro, M. J. (1997). Fractionation of silicon isotopes by marine diatoms during biogenic silica formation. *Geochimica et Cosmochimica Acta*, *61*(23), 5051–5056. https://doi.org/10.1016/S0016-7037(97)00300-1

De La Rocha, C., Brzezinski, M. A., & DeNiro, M. J. (2000). A first look at the distribution of stable isotopes of silicon in natural waters. *Geochimica et Cosmochimica Acta*, *64*(14), 2467–2477. https://doi.org/10.1016/S0016-7037(00)00373-2

de Souza, G. F., Reynolds, B. C., Johnson, G. C., Bullister, J. L., & Bourdon, B. (2012). Silicon stable isotope distribution traces Southern Ocean export of Si to the eastern South Pacific thermocline. *Biogeosciences*, *9*(11), 4199–4213. https://doi.org/10.5194/bg-9-4199-2012

de Souza, G. F., Reynolds, B. C., Rickli, J., & Frank, M. (2012). Southern Ocean control of silicon stable isotope distribution in the deep Atlantic Ocean. *Global Biogeochemical Cycles*, *26*, GB2035. http://doi.org/10.1029/2011GB004141

de Souza, G. F., Slater, R. D., Dunne, J. P., & Sarmiento, J. L. (2014). Deconvolving the controls on the deep ocean's silicon stable isotope distribution. *Earth and Planetary Science Letters*, *398*, 66–76. https://doi.org/10.1016/j.epsl.2014.04.040

Delstanche, S., Opfergelt, S., Cardinal, D., Elsass, F., André, L., & Delvaux, B. (2009). Silicon isotopic fractionation during adsorption of aqueous monosilicic acid onto iron oxide. *Geochimica et Cosmochimica Acta*, *73*(4), 923–934. https://doi.org/10.1016/j.gca.2008.11.014

Demarest, M. S., Brzezinski, M. A., & Beucher, C. P. (2009). Fractionation of silicon isotopes during biogenic silica dissolution. *Geochimica et Cosmochimica Acta*, *73*(19), 5572–5583. https://doi.org/10.1016/j.gca.2009.06.019

Douthitt, C. B. (1982). The geochemistry of the stable isotopes of silicon. *Geochimica et Cosmochimica Acta*, *46*(8), 1449–1458. https://doi.org/10.1016/0016-7037(82)90278-2

Echevin, V., Aumont, O., Ledesma, J., & Flores, G. (2008). The seasonal cycle of surface chlorophyll in the Peruvian upwelling system: A modeling study. *Progress in Oceanography*, *79*(2–4), 167–176. https://doi.org/10.1016/j.pocean.2008.10.026

Ehlert, C., Doering, K., Wallmann, K., Scholz, F., Sommer, S., Grasse, P., et al. (2016). Stable silicon isotope signatures of marine pore waters—Biogenic opal dissolution versus authigenic clay mineral formation. *Geochimica et Cosmochimica Acta*, *191*, 102–117. https://doi.org/10.1016/j.gca.2016.07.022

Ehlert, C., Grasse, P., Mollier-Vogel, E., Böschen, T., Franz, J., Souza, G., et al. (2012). Factors controlling the silicon isotope distribution in waters and surface sediments of the Peruvian coastal upwelling. *Geochimica et Cosmochimica Acta*, *99*, 128–145. https://doi.org/10.1016/j.gca.2012.09.038

Elderfield, H., & Schultz, A. (1996). Mid-ocean ridge hydrothermal fluxes and the chemical composition of the ocean. *Annual Review of Earth and Planetary Sciences*, *24*(1), 191–224. https://doi.org/10.1146/annurev.earth.24.1.191

Estrada, M., & Blasco, D. (1985). Phytoplankton assemblages in coastal upwelling areas.

Feely, R., Geiselman, T., Baker, E., Massoth, G., & Hammond, S. (1990). Distribution and composition of hydrothermal plume particles from the ASHES Vent Field at Axial Volcano, Juan de Fuca Ridge. *Journal of Geophysical Research*, *95*(B8), 12,855–12,873. https://doi.org/10.1029/JB095iB08p12855

Feely, R. A., Gendron, J. F., Baker, E. T., & Lebon, G. T. (1994). Hydrothermal plumes along the East Pacific Rise, 8°40′ to 11°50′ N: Particle distribution and composition. *Earth and Planetary Science Letters*, *128*(1–2), 19–36. https://doi.org/10.1016/0012-821X(94)90023-X

Fitzsimmons, J., John, S., Marsay, C., Hoffman, C., Nicholas, S., Toner, B., et al. (2017). Iron persistence in a distal hydrothermal plume supported by dissolved–particulate exchange. *Nature Geoscience*, *10*(3), 195–201. https://doi.org/10.1038/ngeo2900

Franck, V. M., Bruland, K. W., Hutchins, D. A., & Brzezinski, M. A. (2003). Iron and zinc effects on silicic acid and nitrate uptake kinetics in three high-nutrient, low-chlorophyll (HNLC) regions. *Marine Ecology Progress Series*, *252*, 15–33. https://doi.org/10.3354/meps252015

Franz, J., Krahmann, G., Lavik, G., Grasse, P., Dittmar, T., & Riebesell, U. (2012). Dynamics and stoichiometry of nutrients and phytoplankton in waters influenced by the oxygen minimum zone in the eastern tropical Pacific. *Deep-Sea Research Part I-Oceanographic Research Papers*, *62*, 20–31. https://doi.org/10.1016/j.dsr.2011.12.004

Gao, S., Wolf Gladrow, D. A., & Völker, C. (2016). Simulating the modern δ^{30}Si distribution in the oceans and in marine sediments. *Global Biogeochemical Cycles*, *30*, 120–133. http://doi.org/10.1002/2015GB005189

Geilert, S., Vroon, P. Z., Keller, N. S., Gudbrandsson, S., Stefánsson, A., & Van Bergen, M. J. (2015). Silicon isotope fractionation during silica precipitation from hot-spring waters: Evidence from the Geysir geothermal field, Iceland. *Geochimica et Cosmochimica Acta*, *164*(C), 403–427. https://doi.org/10.1016/j.gca.2015.05.043

Gordon, L. I., Jennings Jr., J. C., Ross, A. A., Krest, J. M. (1992). A suggested protocol for continuous flow automated analysis of seawater nutrients in the WOCE Hydrographic Program and the Joint Global Ocean Fluxes Study. Grp Tech Rpt 92-1. OSU College of Oceanography Descr. Chem Oc.

Grasse, P., Brzezinski, M. A., Cardinal, D., de Souza, G. F., Andersson, P., Closset, I., et al. (2017). GEOTRACES inter-calibration of the stable silicon isotope composition of dissolved silicic acid in seawater. *Journal of Analytical Atomic Spectrometry*, *32*(3), 562–578. https://doi.org/10.1039/C6JA00302H

Grasse, P., Ehlert, C., & Frank, M. (2013). The influence of water mass mixing on the dissolved Si isotope composition in the Eastern Equatorial Pacific. *Earth and Planetary Science Letters*, *380*, 60–71. https://doi.org/10.1016/j.epsl.2013.07.033

Grasse, P., Ryabenko, E., Ehlert, C., Altabet, M. A., & Frank, M. (2016). Silicon and nitrogen cycling in the upwelling area off Peru: A dual isotope approach. *Limnology and Oceanography*, *61*(5), 1661–1676. https://doi.org/10.1002/lno.10324

Hendry, K. R., & Brzezinski, M. A. (2014). Using silicon isotopes to understand the role of the Southern Ocean in modern and ancient biogeochemistry and climate. *Quaternary Science Reviews*, *89*, 13–26. https://doi.org/10.1016/j.quascirev.2014.01.019

Holzer, M., & Brzezinski, M. A. (2015). Controls on the silicon isotope distribution in the ocean: New diagnostics from a data-constrained model. *Global Biogeochemical Cycles*, *29*, 267–287. https://doi.org/10.1002/2014GB004967

Holzer, M., Primeau, F. W., DeVries, T., & Matear, R. (2014). The Southern Ocean silicon trap: Data-constrained estimates of regenerated silicic acid, trapping efficiencies, and global transport paths. *Journal of Geophysical Research: Oceans*, *119*, 313–331. https://doi.org/10.1002/2013jc009356

Hutchins, D. A., & Bruland, K. W. (1998). Iron-limited diatom growth and Si:N uptake ratios in a coastal upwelling regime. *Nature*, *393*(6685), 561–564. https://doi.org/10.1038/31203

Jenkins, W., Lott, D., German, C., Cahill, K., Goudreau, J., & Longworth, B. (2018). The deep distributions of helium isotopes, radiocarbon, and noble gases along the U.S. GEOTRACES East Pacific Zonal Transect (GP16). *Marine Chemistry*, *201*, 167–182. https://doi.org/10.1016/j.marchem.2017.03.009

John, D. G., Helgoe, J., & Twonsend, E. (2017). Geogeochemical cycling of Zn and Cd and their stable isotopes in the eastern Tropical South Pacific. *Marine Chemistry*, *201*, 256–262.

John, S. G., Helgoe, J., Townsend, E., Weber, T., DeVries, T., Tagliabue, A., et al. (2018). Biogeochemical cycling of Fe and Fe stable isotopes in the Eastern Tropical South Pacific. *Marine Chemistry*, *201*, 66–76. https://doi.org/10.1016/j.marchem.2017.06.003

Johnson, H. P., Hautala, S. L., Bjorklund, T. A., & Zarnetske, M. R. (2006). Quantifying the North Pacific silica plume. *Geochemistry, Geophysics, Geosystems*, *7*, Q05011. https://doi.org/10.1029/2005GC001065

Kalvelage, T., Lavik, G., Lam, P., Contreras, S., Arteaga, L., Löscher, C. R., et al. (2013). Nitrogen cycling driven by organic matter export in the South Pacific oxygen minimum zone. *Nature Geoscience*, *6*(3), 228–234. https://doi.org/10.1038/ngeo1739

Karl, D., & Tien, G. (1992). MAGIC: A sensitive and precise method for measuring dissolves phosphorus in aquatic environments. *Limnology and Oceanography*, *37*(1), 105–116. https://doi.org/10.4319/lo.1992.37.1.0105

Karstensen, J., Stramma, L., & Visbeck, M. (2008). Oxygen minimum zones in the eastern tropical Atlantic and Pacific oceans. *Progress in Oceanography*, *77*(4), 331–350. https://doi.org/10.1016/j.pocean.2007.05.009

Kawabe, M., & Fujio, S. (2010). Pacific Ocean Circulation based on observation. *Journal of Oceanography*, *66*(3), 389–403. https://doi.org/10.1007/s10872-010-0034-8

Kleine, B. I., Stefánsson, A., Halldórsson, S. A., Whitehouse, M. J., & Jónasson, K. (2018). Silicon and oxygen isotopes unravel quartz formation processes in the Icelandic crust. *Geochemical Perspectives Letters*, *7*, 5–11. https://doi.org/10.7185/geochemlet.1811

Lam, P. J., Lee, J.-M., Heller, M. I., Mehic, S., Xiang, Y., & Bates, N. R. (2018). Size-fractionated distributions of suspended particle concentration and major phase composition from the U.S. GEOTRACES Eastern Pacific Zonal Transect (GP16). *Marine Chemistry*, *201*, 90–107. https://doi.org/10.1016/j.marchem.2017.08.013

Liguori, B., Ehlert, C., & Pahnke, K. (2020). The influence of water mass mixing and particle dissolution on the silicon cycle in the Central Arctic Ocean. *Frontiers in Marine Science*, *7*, 202. https://doi.org/10.3389/fmars.2020.00202

Meyerink, S. W., Ellwood, M. J., Maher, W. A., Dean Price, G., & Strzepek, R. F. (2017). Effects of iron limitation on silicon uptake kinetics and elemental stoichiometry in two Southern Ocean diatoms, Eucampia antarctica and Proboscia inermis, and the temperate diatom Thalassiosira pseudonana. *Limnology and Oceanography*, *62*(6), 2445–2462. https://doi.org/10.1002/lno.10578

Milligan, A. J., Varela, D. E., Brzezinski, M. A., & Morel, F. M. M. (2004). Dynamics of silicon metabolism and silicon isotopic discrimination in a marine diatomas a function of $p\text{CO}_2$. *Limnology and Oceanography*, *49*(2), 322–329. https://doi.org/10.4319/lo.2004.49.2.0322

Montes, I., Colas, F., Capet, X., & Schneider, W. (2010). On the pathways of the equatorial subsurface currents in the eastern equatorial Pacific and their contributions to the Peru-Chile Undercurrent. *Journal of Geophysical Research: Oceans*, *115*, C09003. https://doi.org/10.1029/2009JC005710

Morel, A., Claustra, H., & Gentili, B. (2010). The most oligotrophic subtropical zones of the global ocean: Similarities and differences in terms of chlorophyll and yellow substance. *Biogeosciences*, *7*(10), 3139–3151. https://doi.org/10.5194/bg-7-3139-2010

Mortlock, R. A., Froelich, P. N., Feely, R. A., Massoth, G. J., Butterfield, D. A., & Lupton, J. E. (1993). Silica and germanium in Pacific Ocean hydrothermal vents and plumes. *Earth and Planetary Science Letters*, *119*(3), 365–378. https://doi.org/10.1016/0012-821X(93)90144-X

Nelson, D., Tréguer, P. J., Brzezinski, M. A., Leynaert, A., & Queguiner, B. (1995). Production and dissolution of biogenic silica in the ocean: Revised global estimates, comparison with regional data and relationship to biogenic sedimentation. *Global Biogeochemical Cycles*, *9*(3), 359–372. https://doi.org/10.1029/95GB01070

Nelson, D. M., & Brzezinski, M. A. (1997). Diatom growth and productivity in an oligo-trophic midocean gyre: A 3-yr record from the Sargasso Sea near Bermuda. *Limnology and Oceanography*, *42*(3), 473–486. https://doi.org/10.4319/lo.1997.42.3.0473

Orsi, A., Johnson, G., & Bullister, J. L. (1999). Circulation, mixing, and production of Antarctic Bottom Water. *Progress in Oceanography*, *43*(1), 55–109. https://doi.org/10.1016/S0079-6611(99)00004-X

Paul, D., Skrzypek, G., & Forizs, I. (2007). Normalization of measured stable isotopic compositions to isotope reference scales—A review. *Rapid Communications in Mass Spectrometry*, *21*(18), 3006–3014. https://doi.org/10.1002/rcm.3185

Pennington, J. T., Mahoney, K. L., Kuwahara, V. S., Kolber, D. D., Calienes, R., & Chavez, F. P. (2006). Primary productivity in the eastern tropical Pacific: A review. *Progress in Oceanography*, *69*(2-4), 285–317. https://doi.org/10.1016/j.pocean.2006.03.012

Peters, B. D., Jenkins, W. J., Swift, J. H., German, C. R., Moffett, J. W., Cutter, G. A., et al. (2018). Water mass analysis of the 2013 US GEOTRACES Eastern Pacific Zonal Transect (GP16). *Marine Chemistry*, *201*, 6–19. https://doi.org/10.1016/j.marchem.2017.09.007

Peters, B. D., Lam, P. J., & Casciotti, K. L. (2018). Nitrogen and oxygen isotope measurements of NO_3^- along the US GEOTRACES Eastern Pacific Zonal Transect (GP16) yield insights into nitrate supply, remineralization, and water mass transport. *Marine Chemistry*, *201*, 137–150. https://doi.org/10.1016/j.marchem.2017.09.009

Ragueneau, O., Tréguer, P., Leynaert, A., Anderson, R. F., Brzezinski, M. A., DeMaster, D. J., et al. (2000). A review of the Si cycle in the modern ocean: Recent progress and missing gaps in the application of biogenic opal as a paleoproductivity proxy. *Global and Planetary Change*, *26*(4), 317–365. https://doi.org/10.1016/S0921-8181(00)00052-7

Resing, J. A., Sedwick, P. N., German, C. R., Jenkins, W. J., Moffett, J. W., Sohst, B. M., & Tagliabue, A. (2015). Basin-scale transport of hydrothermal dissolved metals across the South Pacific Ocean. *Nature*, *523*(7559), 200–203. https://doi.org/10.1038/nature14577

Reynolds, B., Frank, M., & Halliday, A. (2006). Silicon isotope fractionation during nutrient utilization in the North Pacific. *Earth and Planetary Science Letters*, *244*(1–2), 431–443. https://doi.org/10.1016/j.epsl.2006.02.002

Reynolds, B. C. (2009). Modeling the modern marine δ^{30}Si distribution. *Global Biogeochemical Cycles*, *23*, GB2015. https://doi.org/10.1029/2008GB003266

Reynolds, B. C., Aggarwal, J., Andr, L., Baxter, D., Beucher, C., Brzezinski, M. A., et al. (2007). An inter-laboratory comparison of Si isotope reference materials. *Journal of Analytical Atomic Spectrometry*, *22*(5), 561–568. https://doi.org/10.1039/B616755A

Sarmiento, J. L., Gruber, N., Brzezinski, M. A., & Dunne, J. P. (2004). High-latitude controls of thermocline nutrients and low latitude biological productivity. *Nature*, *427*(6969), 57–60. https://doi.org/10.1038/nature02127

Savage, P. S., Georg, R. B., Armytage, R. M. G., Williams, H. M., & Halliday, A. N. (2010). Silicon isotope homogeneity in the mantle. *Earth and Planetary Science Letters*, *295*(1–2), 139–146. https://doi.org/10.1016/j.epsl.2010.03.035

Schlitzer, R. (2018). Ocean Data View. http://odv.awi.de

Schlitzer, R., Anderson, R. F., Dodas, E. M., Lohan, M., Geibert, W., Tagliabue, A., et al. (2018). The GEOTRACES intermediate data product 2017. *Chemical Geology*, *493*, 210–223. https://doi.org/10.1016/j.chemgeo.2018.05.040

Silva, N., Rojas, N., & Fedele, A. (2009). Water masses in the Humboldt Current System: Properties, distribution, and the nitrate deficit as a chemical water mass tracer for Equatorial Subsurface Water off Chile. *Deep Sea Research Part II: Topical Studies in Oceanography*, *56*(16), 1004–1020. https://doi.org/10.1016/j.dsr2.2008.12.013

Sun, X., Olofsson, M., Andersson, P. S., Fry, B., Legrand, C., Humborg, C., & Mörth, C. M. (2014). Effects of growth and dissolution on the fractionation of silicon isotopes by estuarine diatoms. *Geochimica et Cosmochimica Acta*, *130*, 156–166. https://doi.org/10.1016/j.gca.2014.01.024

Sutton, J., André, L., Cardinal, D., Conley, D., Souza, G., Dean, J., et al. (2018). A review of the stable isotope bio-geochemistry of the global silicon cycle and its associated trace elements. *Frontiers in Earth Science*, *5*, 112. https://doi.org/10.3389/feart.2017.00112

Sutton, J. N., Varela, D. E., Brzezinski, M. A., & Beucher, C. P. (2013). Species-dependent silicon isotope fractionation by marine diatoms. *Geochimica et Cosmochimica Acta*, *104*, 300–309. https://doi.org/10.1016/j.gca.2012.10.057

Talley, L. D. (2008). Freshwater transport estimates and the global overturning circulation: Shallow, deep and throughflow components. *Progress in Oceanography*, *78*(4), 257–303. https://doi.org/10.1016/j.pocean.2008.05.001

Thomsen, S., Kanzow, T., Krahmann, G., Greatbatch, R. J., Dengler, M., & Lavik, G. (2016). The formation of a subsurface anticyclonic eddy in the Peru-Chile Undercurrent and its impact on the near-coastal salinity, oxygen, and nutrient distributions. *Journal of Geophysical Research: Oceans*, *121*, 476–501. https://doi.org/10.1002/2015JC010878

Tréguer, P., Bowler, C., Moriceau, B., Dutkiewicz, S., Gehlen, M., Aumont, O., & Jahn, O. (2017). Influence of diatom diversity on the ocean biological carbon pump. *Nature Geoscience*, *11*(1), 27.

Tréguer, P. J., & De La Rocha, C. L. (2013). The world ocean silica cycle. *Annual Review of Marine Science*, *5*(1), 477–501. https://doi.org/10.1146/annurev-marine-121211-172346

Werner, D. (1977). *The biology of diatoms*. Botanical Monographs, 13, University of California Press. Berkeley & Los Angeles.

Wetzel, F., De Souza, G. F., & Reynolds, B. C. (2014). What controls silicon isotope fractionation during dissolution of diatom opal? *Geochimica et Cosmochimica Acta*, *131*, 128–137. https://doi.org/10.1016/j.gca.2014.01.028

Wilkerson, F. P., & Dugdale, R. C. (1996). Silicate versus nitrate limitation in the equatorial Pacific estimated from satellite-derived sea-surface temperatures. *Advances in Space Research*, *18*(7), 81–89. https://doi.org/10.1016/0273-1177(95)00951-5

Wischmeyer, A. G., De La Rocha, C. L., Maier-Reimer, E., & Wolf-Gladrow, D. A. (2003). Control mechanisms for the oceanic distribution of silicon isotopes. *Global Biogeochemical Cycles*, *17*(3), 1083. https://doi.org/10.1029/2002GB002022

Young, E. D., Galy, A., & Nagahara, H. (2002). Kinetic and equilibrium mass-dependent isotope fractionation laws in nature and their geochemical and cosmochemical significance. *Geochimica et Cosmochimica Acta*, *66*(6), 1095–1104. https://doi.org/10.1016/S0016-7037(01)00832-8